

# Fully 3D Monte Carlo reconstruction in SPECT: a feasibility study

D Lazaro<sup>1</sup>, Z El Bitar<sup>2</sup>, V Breton<sup>2</sup>, D Hill<sup>3</sup> and I Buvat<sup>1</sup>

<sup>1</sup> UMR 678 INSERM, UPMR, CHU Pitié-Salpêtrière, 91 Boulevard de l'Hôpital, 75634 Paris Cedex 13, France

<sup>2</sup> Laboratoire de Physique Corpusculaire, CNRS/IN2P3, Université Blaise Pascal, 24 Avenue des Landais, 63177 Aubière Cedex 1, France

<sup>3</sup> ISIMA/LIMOS UMR 6158, Computer Science and Modelling Laboratory, Université Blaise Pascal, 24 Avenue des Landais, BP 10125, 63173 Aubière Cedex, France

E-mail: [buvat@imed.jussieu.fr](mailto:buvat@imed.jussieu.fr)

Received 2 January 2005, in final form 25 April 2005

Published 28 July 2005

Online at [stacks.iop.org/PMB/50/3739](http://stacks.iop.org/PMB/50/3739)

## Abstract

In single photon emission computed tomography (SPECT) with parallel hole collimation, image reconstruction is usually performed as a set of bidimensional (2D) analytical or iterative reconstructions. This approach ignores the tridimensional (3D) nature of scatter and detector response function that affects the detected signal. To deal with the 3D nature of the image formation process, iterative reconstruction can be used by considering a 3D projector modelling the 3D spread of photons. In this paper, we investigate the value of using accurate Monte Carlo simulations to determine the 3D projector used in a fully 3D Monte Carlo (F3DMC) reconstruction approach. Given the 3D projector modelling all physical effects affecting the imaging process, the reconstruction problem is solved using the maximum likelihood expectation maximization (MLEM) algorithm. To validate the concept, three data sets were simulated and F3DMC was compared with two other 3D reconstruction strategies using analytical corrections for attenuation, scatter and camera point spread function. Results suggest that F3DMC improves spatial resolution, relative and absolute quantitation and signal-to-noise ratio. The practical feasibility of the approach on real data sets is discussed.

## 1. Introduction

In single photon emission computed tomography (SPECT) with a parallel hole collimator, image reconstruction is most often performed as a set of two-dimensional (2D) analytic or iterative reconstructions. Each 2D reconstruction considers the 2D sinogram associated with a transaxial slice, assuming that photons emitted in a transaxial slice are detected within a single

line of each planar 2D projection. This is an approximation because of the spatial response of the gamma camera and because of the presence of scattered radiation. In the real world, photons emitted in a transaxial slice are not only detected in the projection line facing the slice, but also in neighbouring lines. The proportion of such out-of-plane photons is actually non-negligible. For instance, it has been shown that out-of-plane photons represent on average 21% of the projection counts recorded in a 1.8 cm slice (20% standard energy window) for a water-filled cylinder (22 cm high, 22 cm in diameter) uniformly filled with Tc-99m (Munley *et al* 1991). This contribution of out-of-plane photons increases when the thickness of the slice decreases, e.g. reaches 48% for slices half a centimetre thick. To better satisfy the 2D hypothesis, scattered photons can be subtracted from the projections before reconstruction using multiple energy window methods or deconvolution kernels (Buvat *et al* 1994), but this reduces the sensitivity of the imaging process and enhances the noise level. The finite point spread function can also be partially compensated for using deconvolution or restoration filtering of the projections before reconstruction (King *et al* 1984, Gilland *et al* 1988, Ogawa *et al* 1988, Lewitt *et al* 1989, Glick *et al* 1994). An alternative approach is to deal with the three-dimensional (3D) nature of the problem, using an iterative reconstruction algorithm involving a 3D projector which models the spread of photons in 3D due to scatter and spatial response function. The 3D modelling of the spatial response function can be easily performed by analytical calculations (Floyd *et al* 1988, Tsui *et al* 1988, Formiconi *et al* 1989, Penney *et al* 1990, Zeng *et al* 1991, Beekman *et al* 1993, Gilland *et al* 1994) but its inclusion into the projector yields a large increase in reconstruction time. Several methods have been developed to reduce reconstruction time, like using block-iterative reconstruction algorithms (Kamphuis *et al* 1998), rotator (Yendiki and Fessler 2004) or unmatched projector/backprojector (Zeng and Gullberg 2000). The analytical modelling of 3D scatter response function is more complicated than that of spatial response function, because the scatter response can be different for every location of the volume of interest to be reconstructed. Different methods have been proposed to model the scatter response function: the slab-derived scatter estimation (Frey *et al* 1993, Frey and Tsui 1994, Beekman and Viergever 1995, Beekman *et al* 1996) consists in calculating and storing scatter response tables for a line source placed behind slabs of variable thicknesses, and to adjust the model to various object shapes. The scatter response table occupies only a few megabytes of memory, and makes it possible to model 3D scatter response functions. This method works well for uniform attenuators but presents limitations for non-uniform attenuators (Frey and Tsui 1994, Beekman *et al* 1997). Another approach is based on the calculation of the scatter response by integrating the Klein–Nishina formula for Compton scattering (Riaska *et al* 1996, Wells *et al* 1998). Similar to Monte Carlo based techniques, this approach requires long processing times and large data storage. Another technique, called effective scatter source estimation (ESSE) (Frey and Tsui 1996), is based on the calculation of an effective scatter source which is used to estimate the contribution of scatter to the projections using the same projector as for the primary photons (Kadrmas *et al* 1998, Zeng *et al* 1999, Bai *et al* 2000). This technique yields promising results in reasonable reconstruction times. The concept of using Monte Carlo simulations to estimate the 3D projector was actually proposed early (Floyd *et al* 1986, 1989, Veklerov *et al* 1988, Bowsher and Floyd 1991) but not applied in fully 3D at that time, due to impractical storage and computation time. During the last decade, several acceleration techniques have been developed, making Monte Carlo based reconstruction possibly practical: accelerated iterative algorithms (Hudson and Larkin 1994, Byrne 1996), unmatched projector–backprojector pairs (Welch and Gullberg 1997, Kamphuis *et al* 1998, Zeng and Gullberg 2000), ‘hybrid’ solutions called convolution-based forced detection (De Jong *et al* 2001, Beekman *et al* 2002), combining stochastic photon transport within the patient with analytical modelling of the camera spatial response. The use of

Monte Carlo simulations to calculate the projector has been recently revisited for tomographic reconstruction of data acquired using a positron emission tomograph (PET) dedicated to small animal imaging (Rafecas *et al* 2003, Motta *et al* 2002, Shokouhi *et al* 2004), but again, only 2D reconstruction has been considered. As computer science is evolving fast, fully 3D reconstruction using a projector entirely calculated using Monte Carlo simulations—that we will call F3DMC for ‘Fully 3D Monte Carlo’ in the following—might become feasible soon. The purpose of this paper is threefold: (1) to demonstrate the feasibility of F3DMC in SPECT, (2) to determine the improvement to be expected from F3DMC in ideal conditions, in terms of image quality and quantitative accuracy, compared to more conventional reconstruction approaches, (3) to study the robustness of F3DMC with respect to typical modelling errors.

Section 2 presents the theory of the F3DMC reconstruction approach. Section 3 describes the method used to study the relevance of F3DMC reconstruction on simulated data. Results obtained using F3DMC reconstruction and more conventional reconstruction approaches are presented in section 4 and discussed in section 5.

## 2. Theory

### 2.1. Formulation of the fully 3D reconstruction problem

A discrete expression of the SPECT tomographic reconstruction problem can be as follows:

$$p = \mathbf{R}f, \quad (1)$$

where  $p$  is a column vector with  $P \times N^2$  elements—assuming  $P$  projections of  $N \times N$  pixels are acquired,  $f$  is a column vector of  $N^3$  elements—assuming  $N$  transaxial slices  $N \times N$  are to be estimated—and  $\mathbf{R}$  is a  $(PN^2, N^3)$  matrix corresponding to the fully 3D projector. An element  $r_{ij}$  of projector  $\mathbf{R}$  corresponds to the probability that a photon emitted from voxel  $j$  is detected in projection pixel  $i$ . Because the problem is very large (typically,  $\mathbf{R}$  is a  $262\,144 \times 262\,144$  matrix if  $N = P = 64$ ), it is usually not addressed in its full dimensionality. Instead, it is most often factorized as a set of  $N$  independent reconstruction problems, each involving  $P$  mono-dimensional (1D) projections with  $N$  elements, a 2D object with  $N \times N$  elements corresponding to a transaxial slice and a  $(PN, N^2)$  projector matrix. In the F3DMC approach however, as in all ‘fully 3D’ reconstruction approaches, the problem is dealt with in its full dimensionality, i.e. by considering the  $(PN^2, N^3)$  projector.

### 2.2. Modelling $\mathbf{R}$

To solve the fully 3D reconstruction problem expressed by equation (1), the first step is to model the projector  $\mathbf{R}$ . In F3DMC reconstruction, Monte Carlo simulations are used to estimate  $\mathbf{R}$ , as they currently offer the most precise modelling of all physical effects involved in SPECT.

*2.2.1. Initial calculation of  $\mathbf{R}$ .* The elements of  $\mathbf{R}$  depend on the geometry and attenuating properties of the ‘object’ under investigation, as well as on the characteristics of the imaging system. Assuming the attenuating properties of the object are known, from a CT scan for instance,  $\mathbf{R}$  is estimated by running a Monte Carlo simulation that considers a uniform activity distributed over the attenuating medium. For each detected event, the couple  $(j, i)$  is stored, where  $j$  represents the emission voxel and  $i$  represents the detection pixel. From all detected events, each  $r_{ij}$  element of projector  $\mathbf{R}$  is deduced as the ratio of the number of events emitted in voxel  $j$  and detected in pixel  $i$  over the number of events emitted in voxel  $j$ .  $\mathbf{R}$  can be

calculated for any energy window. For storage savings, the dimension of  $\mathbf{R}$  is not  $(PN^2, N^3)$ , but only  $(PN^2, M)$ , where  $M$  is the number of voxels belonging to the attenuating medium. Indeed, one can assume that only voxels belonging to the attenuating medium contribute to the observed projections.

**2.2.2. Filtering of  $\mathbf{R}$ .** Because  $\mathbf{R}$  is derived from a Monte Carlo simulation, hence from a limited number of photon histories, each element  $r_{ij}$  is an estimate of the true probability value that would be obtained if an infinite number of histories was considered. In other words,  $\mathbf{R}$  is a noisy estimate of the actual projector. To reduce the noise affecting  $\mathbf{R}$ ,  $\mathbf{R}$  is first reorganized as  $P$  sub-matrices  $\mathbf{S}$  of dimensions  $(N^2, M)$ , so that the element  $s_{ij}$  represents the contribution of voxel  $j$  to projection pixel  $i$ . Each of these sub-matrices is related to a specific projection. The elements of the matrix can be set as a vector with  $N^2 \times M$  elements. A principal component analysis (Jolliffe 1992) of the resulting set of  $P$  vectors is performed, yielding a set of  $P$  eigenvalues associated with  $P$  eigenvectors. The first  $K$  eigenvectors associated with the highest  $K$  eigenvalues are considered to recover a filtered version of the original vectors (considering  $K = P$  would yield the original vectors). The resulting filtered vectors are then reorganized into a  $(PN^2, M)$  matrix to get the filtered projector  $\mathbf{R}'$ , supposedly less noisy than the original projector.

### 2.3. Reconstructing the image volume

Given the projector  $\mathbf{R}$  (or  $\mathbf{R}'$ ), the inverse problem  $p = \mathbf{R}f$  can be solved using any classical iterative algorithms. Because the measured projections follow Poisson statistics in SPECT, we used the maximum likelihood expectation maximization (MLEM) (Miller *et al* 1985). The result is the  $f$  column vector with  $M$  elements, representing the activity distribution within the attenuating medium.

## 3. Material and methods

To study the feasibility and the robustness of the F3DMC approach, Monte Carlo simulations were performed using the GATE code ([www.opengatecollaboration.org](http://www.opengatecollaboration.org)). This code has been recently validated for various configurations in SPECT (e.g., Staelens *et al* 2003, Lazaro *et al* 2004, Assié *et al* 2005, Jan *et al* 2004). For each studied phantom, two sets of data were generated using GATE: the projections of the phantom and the projector used for F3DMC reconstruction of the phantom.

### 3.1. Simulated phantoms

Numerical phantoms were described with GATE using an input parameter file, including the description of the phantom geometry, the description of its atomic composition (and thus its attenuation properties) and of the radioactive distribution in the phantom. Three phantoms have been considered (figure 1). The 'sphere phantom' was a water-filled cylinder (10 cm in diameter, 10 cm high), including a 2 cm diameter sphere filled with water. The sphere was centred in the cylinder and a Tc-99m activity of 24 MBq ml<sup>-1</sup> was set in the sphere, while no activity was introduced in the cylinder (figure 1(a)).

The 'line and point phantom' was a 10 cm × 10 cm × 10 cm tank consisting of three layers of air, water and bone along the  $X$  direction (figure 1(b)). This phantom included three line sources and three point sources (figure 1(b)) with no activity in the background. The relative activity concentrations were 6, 8 and 10 in the '1', '2', '3' point sources, respectively, and 10, 15 and 20 in the  $X$ ,  $Y$  and  $Z$  line sources, respectively.

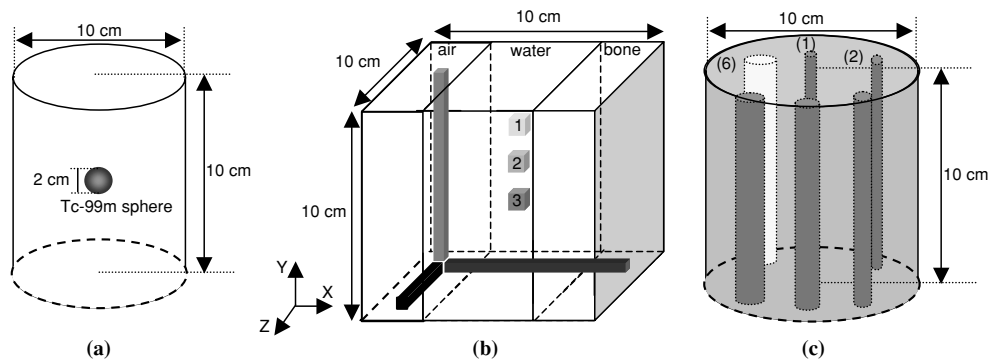


**Figure 1.** Simulated phantoms: (a) ‘sphere phantom’: water cylinder containing a Tc-99m sphere; (b) ‘line and point phantom’: water tank including three attenuating media and Tc-99m line and point sources; (c) ‘cylinder phantom’: water cylinder including five Tc-99m rods of different diameters and a cold bony rod.

**Table 1.** Number of simulated and detected counts for the projections of the three considered phantoms.

Phantom	Number of simulated photons (billion)	Detected counts between 126 and 154 keV
Sphere phantom	3.10	606 698
Line and point phantom	4.71	1151 553
Cylinder phantom	29.16	6211 922

The ‘cylinder phantom’ was a water-filled cylinder (10 cm in diameter, 10 cm high), including six rods (10 cm high) with diameters of 4.8 mm, 6.4 mm, 7.8 mm, 9.5 mm, 11.1 mm and 12.7 mm. The smallest five rods were filled with water whereas the biggest contained bony material. The bony rod contained no activity (‘cold rod’). A background Tc-99m activity of  $2.08 \text{ MBq ml}^{-1}$  ( $C_{\text{background}}$ ) was set within the rest of the cylindrical phantom, except within the five water-filled rods, which contained a Tc-99m activity equal to four times that of the background ( $C_{\text{hot}} = 8.32 \text{ MBq ml}^{-1}$ ) (figure 1(c)).

The ‘sphere phantom’ and the ‘line and point phantom’ volumes were sampled on a  $10 \times 10 \times 10$  voxel grid (voxel size =  $1 \text{ cm} \times 1 \text{ cm} \times 1 \text{ cm}$ ), while the ‘cylinder phantom’ was sampled on a  $64 \times 64 \times 64$  voxel grid (voxel size =  $3.125 \text{ mm} \times 3.125 \text{ mm} \times 3.125 \text{ mm}$ ).

### 3.2. SPECT simulations

For the ‘sphere phantom’ and the ‘line and point phantom’, a SPECT acquisition of 64 projections  $10 \times 10$  (pixel size: 1 cm) was simulated with a 12 cm radius of rotation. For the ‘cylinder phantom’, 64 projections  $64 \times 64$  (pixel size: 3.125 mm) were simulated with a 12 cm radius of rotation. In both cases, the following gamma camera characteristics were included in the input parameter file, to model the response of the AXIS gamma camera (Philips): 8.8% energy resolution at 140 keV, high-resolution collimator and 7.6 mm full width at half maximum (FWHM) system resolution for a point source located at 10 cm from the collimator. The numbers of simulated and detected counts in the projections for the three phantoms are summarized in table 1.

Simulation output was stored in a list-mode file, containing emission and detection positions of each detected photon, as well as the energy at which each photon was detected.

This list-mode file was then processed to create the projections corresponding to the 126–154 keV and 92–125 keV energy windows.

### 3.3. Projector calculation

For the ‘sphere phantom’, a simulation with a uniform Tc-99m activity distribution within the water cylinder was performed. About 10 billion photons were simulated, which corresponds to 10 million photons emitted per voxel, and about 2 million events were detected between 126 and 154 keV. The simulation time was about 457 h on a biprocessor Pentium III 1 GHz machine. As we used a cluster of 40 biprocessors (Pentium III 1 GHz), the simulation actually ran for about 12 h.

For the ‘line and point phantom’, about 30 billion photons corresponding to a uniform Tc-99m activity distribution within the non-uniform attenuating medium were simulated (30 million photons emitted per voxel) and about 6.9 million photons were detected between 126 and 154 keV.

Finally, for the ‘cylinder phantom’, about 75 billion photons corresponding to a uniform Tc-99m activity distribution within the water cylinder were simulated (about 285 000 photons emitted per voxel) and about 16 million photons were detected between 126 and 154 keV. In this latter case, the simulation took about 10 days on our cluster.

For each phantom, the matrix  $\mathbf{R}$  was deduced as explained before. It was entirely stored for the ‘sphere phantom’ and for the ‘line and point phantom’, as its size was only 25.6 Mo ( $P = 64, N = 10, 6.4 \times 10^6$  elements). On the other hand, the full storage of the matrix  $\mathbf{R}$  for the ‘cylinder phantom’ was not conceivable because it would have required several hundred gigabytes. We thus chose to store only nonzero elements of the matrix, which reduced the size of the matrix  $\mathbf{R}$  to about 89 MB, and also reduced the reconstruction time. The projector was filtered using  $K = 14, 16$  and  $48$  for the ‘sphere phantom’, ‘line and point phantom’ and ‘cylinder phantom’, respectively. These  $K$  values were empirically determined as yielding appropriate trade-off between quantitative accuracy and noise level in the reconstructed images. In fact, filtering decreases the noise level in the reconstructed images but also leads to poorer spatial resolution, thus poorer quantitation than unfiltered data. The optimization of filtering thus consisted in finding the smallest  $K$  value (strongest removal of noise) allowing for a good quantitative accuracy.

### 3.4. Image reconstruction

To assess the value of F3DMC reconstruction with respect to other 3D reconstruction methods, data collected in the 126–154 keV energy window were reconstructed using the following three reconstruction methods:

- (1) Filtered backprojection, combined with corrections for scatter, depth-dependent spatial resolution and attenuation (FBP-C). Projections were corrected for scatter using the Jaszczak method, with the 92–125 keV window as the ‘Compton’ energy window and  $k = 0.5$  (Jaszczak *et al* 1984). Projections were then filtered for depth-dependent spatial resolution correction using the frequency–distance principle (Lewitt *et al* 1989). Attenuation correction was then performed using the iterative Chang algorithm (three iterations), with the exact attenuation map considered for simulating the projections (Tsui *et al* 1989).
- (2) MLEM combined with corrections for scatter, attenuation and depth-dependent spatial resolution, denoted as MLEM-C below. The projections were first corrected for scatter using the Jaszczak method, with the 92–125 keV window as the ‘Compton’ energy window

and  $k = 0.5$ . Attenuation and depth-dependent spatial resolution were modelled within the projector used for reconstruction. The attenuation map considered for simulating the projections was considered to model attenuation in the projector. The number of iterations was optimized for each phantom, by selecting the number of iterations at which convergence was achieved, where convergence was defined as mean values measured in regions of interest used for quantitative assessment (see below) remaining unchanged within 1%. Using this convergence criterion, 30 iterations were used for the 'sphere phantom' and the 'line and point phantom', and 80 iterations were used for the 'cylinder phantom'.

- (3) F3DMC, consisting in using the MLEM algorithm to solve the inverse problem described by mean of the 3D projector  $\mathbf{R}$  obtained using 3D Monte Carlo modelling of scatter, attenuation and finite spatial resolution. Thus, as the projector modelled scatter, attenuation and finite spatial resolution, these phenomena were implicitly corrected for when inverting  $p = \mathbf{R}f$ . The number of iterations was optimized for each phantom, by selecting the number of iterations at which convergence was achieved as defined above. Thirty iterations were used for the 'sphere phantom' and the 'line and point phantom', and 60 iterations for the 'cylinder phantom'.

In summary, all reconstruction schemes included corrections for attenuation, scatter and spatial response, but FBP-C and MLEM-C used analytical models for the corrections while F3DMC used Monte Carlo models.

### 3.5. Image assessment

To assess the accuracy of the reconstructed images, several criteria were considered:

- Percentage of 'mislocated' events, calculated for the 'sphere phantom' and defined as the total activity detected outside the eight voxels containing the sphere divided by the total reconstructed activity.
- Spatial resolution, calculated for the 'line and point phantom'. In-plane and axial spatial resolutions were assessed by drawing profiles through the hottest point source (figure 1) in the  $x$  and  $z$  directions, respectively, and by estimating the FWHM from these profiles.
- Relative quantitation. For each line of the 'line and point phantom', an average line activity value was determined by averaging the value of the four hottest pixels (it was checked that similar results were obtained when considering the six hottest values instead of four). The ratios between the average activity measured in the  $Z$  and  $Y$  line sources (theoretical value = 1.33) and between the average activity of the  $Z$  and  $X$  line sources (theoretical value = 2) were considered. For the 'cylinder phantom', the activity ratio between each rod and the background activity was calculated, by considering cylindrical volumes of interest (VOIs) drawn over each rod, with diameters equal to the actual diameter of the different rods and height equal to 20 pixels. A background VOI of 2 pixel diameter and 20 pixel height was drawn between the two smallest hot rods.
- Absolute quantitation. To assess the feasibility of restoring absolute activity values, the percentage of recovered activity (%RA) for each phantom was calculated as follows:  $\%RA = 100 \times (\text{estimated phantom activity}) / (\text{simulated phantom activity})$ . For F3DMC, the phantom activity was directly estimated as the total number of counts in the reconstructed images divided by the simulated acquisition duration. For FBP-C and MLEM-C, phantom activity can only be estimated using a calibration factor. This calibration factor was determined using the 'sphere phantom' and was defined as the number of counts emitted during the simulation divided by the total number of counts

in the reconstructed image. For FBP-C and MLEM-C, two calibration factors  $C_{\text{FBP}}$  and  $C_{\text{MLEM}}$  were calculated considering the total number of counts in the FBP-C and the MLEM-C reconstructed images, respectively. To deduce the ‘estimated phantom activity’ and hence %RA for each phantom, the total number of counts was multiplied by  $C_{\text{FBP}}$  in the FBP-C images and by  $C_{\text{MLEM}}$  in the MLEM-C images.

- Signal-to-noise ratio (SNR). For each of the three phantoms, 20 noisy replicates of the projections were obtained: the mean number of counts in the projections and associated standard deviation were  $606\,745 \pm 253$ ,  $1151\,367 \pm 1003$  and  $6211\,952 \pm 2023$  for the sphere phantom, the cubic phantom and the Jaszczak phantom, respectively. Each replicate was reconstructed using the three reconstruction methods. SNR was defined as the mean number of counts within a VOI (sphere for the ‘sphere phantom’, four hottest pixels of the Z line for the ‘line and point phantom’, background VOI used for relative quantitation for the ‘cylinder phantom’) averaged over the 20 replicates of reconstructed images, divided by the standard deviation of that mean.

### 3.6. Study of the impact of noise in the projector

The impact of the number of simulated counts used to calculate the projector on the reliability of the reconstructed images was studied using the ‘sphere phantom’. Projectors corresponding to 1 billion, 5 billion, 10 billion simulated counts and 10 billion simulated counts filtered using  $K = 14$  were considered.

### 3.7. Study of the robustness of F3DMC with respect to modelling errors

As the same simulation code was used to generate the projections and the projector  $\mathbf{R}$ , F3DMC was expected to perform at its best. When using real data, Monte Carlo simulations never perfectly reproduce experimental configurations, so there will be differences between the unknown projector  $\mathbf{R}$  that yielded the acquired data and the  $\mathbf{R}$  estimated from Monte Carlo simulations. To better assess the value of F3DMC when working on real data, we introduced errors in the modelling of the projector  $\mathbf{R}$  for the ‘line and point phantom’ and for the ‘cylinder phantom’. Two types of errors were considered:

- First, to mimic a 4 keV shift in the energy calibration of the camera, a set of projections  $P_1$  corresponding to data recorded in the 122–150 keV energy range was calculated. The projector appropriate for data recorded in the 126–154 keV energy range was applied to data recorded in the 122–150 keV energy range. Such a shift would actually also affect MLEM-C through scatter correction: instead of subtracting the weighted 92–125 keV data from the 126–154 keV data, the poor energy calibration of the camera would lead to the subtraction of the 88–121 keV data from the 122–150 keV data. In addition, for attenuation correction, the attenuation map scaled for 140 keV would actually be applied to data detected at 136 keV (and same shift for all energy values). Such erroneous processing scheme was therefore reproduced for MLEM-C (yielding MLEM-C1), to compare the results with those of MLEM-C without modelling errors and with those of F3DMC without and with modelling errors.
- Second, a shift in spatial sampling was introduced, by computing sets of projections after shifting horizontally and vertically the pixel sampling grid with respect to the grid used for calculating the projector. For the ‘line and point phantom’, projections were shifted by almost a quarter of a pixel (2 mm) or half of a pixel (5 mm), and referred to as  $P_2$  and  $P_3$  in the following. For the ‘cylinder phantom’, projections were shifted by half of a pixel (1.56 mm), one pixel (3.125 mm) and two pixels (6.25 mm) and referred to as  $P_2$ ,

**Table 2.** Quantitative criteria characterizing the ‘sphere phantom’ images as a function of the reconstruction method.

Reconstruction method	Percentage of	
	mislocated events	SNR
FBP-C	2.0	640
MLEM-C	1.9	800
F3DMC + PCA filtering	1.7	826

$P_3$  and  $P_4$ . Such shift would typically be encountered if the CT-derived attenuation map used as an input for the Monte Carlo simulation from which the projector is deduced was slightly misaligned with the acquired emission data. In that case, MLEM-C reconstruction would also be affected by the shift. We thus also performed MLEM-C using attenuation maps affected by the same shifts as those in  $P_2$ ,  $P_3$  and  $P_4$ , noted hereafter MLEM-C2, MLEM-C3 and MLEM-C4.

In addition, projections of the ‘cylinder phantom’ ( $P_{\text{SIMSET}}$ ) were simulated using the Monte Carlo simulation package SimSET (Harrison *et al* 1993) and reconstructed with MLEM-C and F3DMC using the filtered version of the projector estimated with GATE. The modelling of the camera response in SimSET was as close as possible to the modelling used in GATE, the major difference being that SimSET included an analytical modelling of the collimator response while in GATE, photon transport in the collimator is modelled using the Monte Carlo approach.

In all cases, F3DMC reconstructions of the different sets of projections ( $P_1$ ,  $P_2$ ,  $P_3$ ,  $P_4$ ,  $P_{\text{SIMSET}}$ ) that included modelling errors were performed with the filtered projector  $\mathbf{R}$ , and were compared to F3DMC reconstruction performed with the set of projections  $P$ , which did not include any modelling error, and with MLEM-C without and with modelling errors. These comparisons were performed in terms of spatial resolution, relative and absolute quantitation and SNR, as described in section 3.6.

## 4. Results

### 4.1. Phantom results

For the ‘sphere phantom’, the percentage of mislocated events and SNR results obtained for the three reconstruction methods are summarized in table 2.

For the ‘line and point phantom’, the in-plane and axial spatial resolution, relative and absolute quantitation indices and SNR are given in table 3.

For the ‘cylinder phantom’, the relative and absolute quantitation indices and the SNR are given in table 4. Activity ratios measured on the original activity images used for the simulation are also shown, to separate the effect of sampling bias from the effect of reconstruction bias. Images reconstructed using the three reconstruction approaches are shown in figure 2, each image being scaled so that its maximum value corresponds to the maximum value of the grey scale.

### 4.2. Impact of the noise in the projector

Table 5 summarizes the impact of the number of simulated counts used to calculate the projector on the reconstructed images of the ‘sphere phantom’ and the impact of filtering.

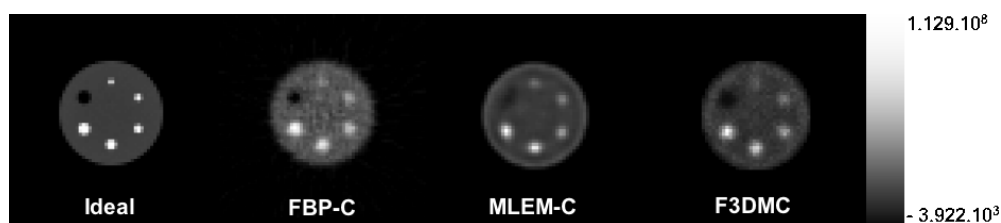


**Figure 2.** Ideal image and reconstructed images of the 'cylinder phantom' using the three reconstruction approaches.

**Table 3.** Quantitative criteria characterizing the 'line and point phantom' images as a function of the reconstruction method. Per cent errors with respect to the true values (line 'ideal') are given in parenthesis.

Reconstruction method	Spatial resolution (in plane/axial)	Relative quantitation Z:Y	Relative quantitation Z:X	Absolute quantitation (%RA)	SNR
Ideal	1.00/1.00	1.33	2.00	100	–
FBP-C	1.25/1.21	0.96 (–27.9%)	1.27 (–36.5%)	96.8	234
MLEM-C	1.13/1.06	1.35 (1.5%)	2.18 (9.0%)	90.9	249
F3DMC+PCA filtering	1.03/1.01	1.33 (0%)	1.77 (–11.5%)	99.5	247

**Table 4.** Quantitative criteria characterizing the 'cylinder phantom' images as a function of the reconstruction method. Per cent errors with respect to the values obtained on the original sampled images (line 'after sampling') are given in parenthesis.

Reconstruction method	Relative quantitation						Absolute quantitation (%)	SNR
	cyl 1	cyl 2	cyl 3	cyl 4	cyl 5	cyl 6		
Ideal	4.00	4.00	4.00	4.00	4.00	0.00	–	–
After sampling	1.92	2.23	2.46	2.54	2.73	0.41	100	–
FBP-C	1.55 ± 0.05 (–19.3%)	1.81 ± 0.05 (–18.8%)	1.98 ± 0.06 (–19.5%)	2.27 ± 0.07 (–10.6%)	2.44 ± 0.07 (–10.6%)	0.49 ± 0.02 (19.5%)	90.0	39
MLEM-C	1.61 ± 0.03 (–16.2%)	1.80 ± 0.04 (–19.3%)	1.93 ± 0.04 (–21.5%)	2.47 ± 0.07 (–2.8%)	2.46 ± 0.05 (–9.9%)	0.71 ± 0.02 (73.2%)	84.2	44
F3DMC+PCA filtering	1.68 ± 0.06 (–12.5%)	2.04 ± 0.07 (–8.5%)	2.33 ± 0.07 (–5.3%)	2.82 ± 0.07 (11.0%)	3.01 ± 0.07 (10.3%)	0.45 ± 0.02 (8.9%)	98.6	43

**Table 5.** Quantitative criteria characterizing the 'sphere' images as a function of the projector used in the F3DMC method.

Number of simulated counts used to calculate the projector	Percentage of mislocated events (%)	Absolute quantitation (%RA)	SNR
1 billion	24.9	93.6	603
5 billion	11.3	97.4	761
10 billions	7.7	98.4	783
10 billions + PCA filtering	1.7	98.4	826

**Table 6.** Quantitative criteria characterizing the ‘line and point phantom’ images with respect to modelling errors. Per cent errors with respect to the true values (line ‘ideal’) are given in parenthesis.

Reconstruction method	Spatial resolution (in-plane/axial)	Relative quantitation Z:Y	Relative quantitation Z:X	Absolute quantitation (%RA)	SNR
Ideal	1.00/1.00	1.33	2.00	100	–
F3DMC (P)	1.03/1.01	1.33 (0%)	1.77 (–11.5%)	99.5	247
F3DMC ( $P_1$ )	1.03/1.01	1.32 (–0.8%)	1.82 (–9.9%)	99.7	257
FD3MC ( $P_2$ )	1.06/1.07	1.46 (9.8%)	1.76 (–12%)	96.6	181
FD3MC ( $P_3$ )	1.43/2.00	2.15 (61.7%)	1.65 (–17.5%)	93.2	102
MLEM-C (P)	1.13/1.06	1.35 (1.5%)	2.18 (9%)	90.9	249
MLEM-C1 ( $P_1$ )	1.14/1.07	1.30 (–2.3%)	2.05 (2.5%)	92.3	194
MLEM-C2 ( $P_2$ )	1.17/1.21	1.42 (6.8%)	2.40 (20%)	92.2	215
MLEM-C3 ( $P_3$ )	1.56/2.00	1.68 (26.3%)	2.75 (37.5%)	91.5	129

#### 4.3. Robustness of F3DMC as a function of modelling errors

Table 6 summarizes the impact of modelling errors in F3DMC and MLEM-C upon the criteria used for image assessment of the ‘line and point phantom’ images.

Table 7 gives the corresponding results for the ‘cylinder phantom’.

## 5. Discussion

### 5.1. Practical feasibility of F3DMC approach

Because of the huge size of the projector involved in the inverse problem to be solved, projector storage and computation time are two main issues of F3DMC reconstruction. For instance, the projector needed to reconstruct the ‘cylinder phantom’ includes  $64^6$  elements ( $64$  projections  $64 \times 64$  used to reconstruct a  $64 \times 64 \times 64$  volume), which requires about 137 GB for storage in integer (assuming that the denominator, i.e. the number of simulated photons per voxel, is stored separately and is then used to compute  $r_{ij}$  elements). By storing only nonzero elements, the projector computed with 75 billion photon emitted requires only about 89 MB, which makes the projector easily tractable.

The computation time includes both the Monte Carlo simulation duration and the reconstruction time. Several days of CPU are currently needed for simulating the projector corresponding to a patient acquisition with GATE, even when using a cluster of PC. The simulation of the ‘cylinder phantom’ projector requires 10 days CPU using a cluster of 40 biprocessors (Pentium III 1 GHz). As computer science is evolving fast, Monte Carlo simulation time should be drastically reduced in the near future. Faster Monte Carlo simulation codes (e.g., SimSET) could also be used instead of GATE, when using radioisotopes such as Tc-99m, for which analytical modelling of the collimator response is accurate enough to model the detector response. For the ‘cylinder phantom’ we estimated that it should take about 10 min (on a single biprocessor PC) with SimSET to compute a projector similar in terms of statistics to that estimated with GATE.

Reconstruction time depends on the iterative reconstruction algorithm. For the ‘cylinder phantom’, reconstruction took 11 min CPU for 60 MLEM iterations on an Intel Xeon 2.8 GHz with 512 kB of cache memory. Using OSEM instead of MLEM will make it possible to reduce this time by a factor of 16 at least.

**Table 7.** Quantitative criteria characterizing the ‘cylinder phantom’ images with respect to modelling errors. Per cent errors with respect to the values measured on the original sampled images (line ‘after sampling’) are given in parenthesis.

Reconstruction method	Relative quantitation						Absolute quantitation (%)	SNR
	cyl 1	cyl 2	cyl 3	cyl 4	cyl 5	cyl 6		
After sampling	1.92	2.23	2.46	2.54	2.73	0.41	100%	–
F3DMC (P)	1.68 ± 0.06 (–12.5%)	2.04 ± 0.07 (–8.5%)	2.33 ± 0.07 (–5.3%)	2.82 ± 0.07 (11.0%)	3.01 ± 0.07 (10.3%)	0.45 ± 0.02 (8.9%)	98.6	43
F3DMC (P <sub>1</sub> )	1.57 ± 0.07 (–18.3%)	1.93 ± 0.07 (–13.5%)	2.22 ± 0.08 (–9.8%)	2.64 ± 0.10 (3.9%)	2.86 ± 0.09 (4.8%)	0.47 ± 0.02 (14.7%)	98.6	33
F3DMC (P <sub>2</sub> )	1.55 ± 0.06 (–19.3%)	1.93 ± 0.06 (–13.5%)	2.16 ± 0.06 (–12.2%)	2.62 ± 0.08 (3.2%)	2.79 ± 0.09 (2.2%)	0.45 ± 0.02 (9.8%)	98.2	38
F3DMC (P <sub>3</sub> )	1.42 ± 0.08 (–26.1%)	1.61 ± 0.06 (–27.8%)	1.90 ± 0.07 (–22.8%)	2.26 ± 0.09 (–11.1%)	2.43 ± 0.10 (–11.0%)	0.54 ± 0.03 (31.7%)	97.8	27
F3DMC (P <sub>4</sub> )	0.72 ± 0.03 (–62.5%)	0.86 ± 0.03 (–61.5%)	0.91 ± 0.02 (–63.0%)	0.96 ± 0.03 (–62.2%)	1.08 ± 0.03 (–60.5%)	0.63 ± 0.02 (53.7%)	97.1	50
FD3MC (P <sub>SIMSET</sub> )	1.79 ± 0.05 (–6.8%)	2.09 ± 0.05 (–6.3%)	2.28 ± 0.05 (–7.3%)	3.05 ± 0.07 (20.0%)	3.21 ± 0.07 (17.6%)	0.37 ± 0.02 (–9.8%)	60.8	49
MLEM-C (80it)	1.61 ± 0.03 (–16.2%)	1.80 ± 0.04 (–19.3%)	1.93 ± 0.04 (–21.5%)	2.47 ± 0.07 (–2.8%)	2.46 ± 0.05 (–9.9%)	0.71 ± 0.02 (73.2%)	84.2	44
MLEM-C1	1.41 ± 0.05 (–26.6%)	1.75 ± 0.07 (–21.5%)	1.97 ± 0.07 (–19.9%)	2.15 ± 0.08 (–39.0%)	2.28 ± 0.09 (–16.5%)	0.79 ± 0.03 (92.7%)	83.4	28
MLEM-C2	1.38 ± 0.06 (–39.2%)	1.68 ± 0.06 (–24.7%)	1.72 ± 0.07 (–30.1%)	2.05 ± 0.08 (–19.3%)	2.01 ± 0.07 (–26.4%)	0.73 ± 0.03 (78.1%)	81.6	28
MLEM-C3	1.15 ± 0.04 (–40.1%)	1.37 ± 0.07 (–38.6%)	1.41 ± 0.06 (–42.7%)	1.71 ± 0.07 (–32.7%)	1.69 ± 0.05 (–38.1%)	0.80 ± 0.03 (95.2%)	81.2	30
MLEM-C4	0.90 ± 0.04 (–53.2%)	0.87 ± 0.04 (–61.0%)	0.98 ± 0.04 (–60.2%)	1.03 ± 0.04 (–59.5%)	1.08 ± 0.05 (–60.4%)	1.07 ± 0.04 (161.0%)	79.8	28

## 5.2. Phantom results

For the ‘sphere phantom’ (table 2), results obtained with F3DMC were as good as and even better than those obtained with the two other 3D analytical reconstruction methods, in terms of percentage of mislocated events. SNR is improved by more than 25% when using 3D iterative reconstruction methods (MLEM-C and F3DMC) compared to FBP-C.

For the ‘line and point phantom’ (table 3), F3DMC yielded almost perfect spatial resolution restoration in reconstructed images. Relative quantitation was more accurate with F3DMC and MLEM-C than with FBP-C. Absolute quantitation results suggested that F3DMC makes it possible to assess accurately the radioisotope concentration values in the reconstructed images, without needing any calibration procedure. Even if such a calibration procedure is

conducted for FBP-C and MLEM-C reconstruction methods, it yields less accuracy in the assessment of radioisotope concentration values. This is because the sensitivity of the system is accurately modelled in the projector for F3DMC, taking into account the count loss due to the collimator. Reconstructed images with MLEM-C and F3DMC are characterized by a similar signal-to-noise ratio.

For the 'cylinder phantom' (table 4), an important loss in quantitative accuracy was introduced by the sampling of the activity distribution onto a voxel matrix. Indeed, the very sampling of the activity distribution (without considering any reconstruction step) made the activity ratios measured on the sampled images much smaller than the actual activity ratios (55% smaller for the smallest rod and 33% smaller for the largest rod). Considering the values measured on the simulated sampled activity maps as reference values for assessing the accuracy of activity ratio restoration, the best accuracy was observed with F3DMC and FBP-C. The average error on activity ratio estimates over all hot rods was about 17%, 24% and 10%, for FBP-C, MLEM-C and F3DMC, respectively. F3DMC also yielded the smallest activity value in the cold rod, compared to the other two reconstruction approaches. Figure 2 illustrates the high contrast obtained in the F3DMC image. Similar to what was observed for the 'line and point phantom', F3DMC performed better than FBP-C and MLEM-C in terms of absolute quantitation. Finally, signal-to-noise ratio was similar for F3DMC and MLEM-C, and was improved by about 10% compared to FBP-C.

In summary, F3DMC reconstruction yielded a better spatial resolution in reconstructed images than alternative reconstruction approaches, as well as improved quantitative accuracy (both for relative and absolute quantitation). Results were especially impressive for the cold rod of the 'cylinder phantom'. Furthermore, results obtained with F3DMC reconstruction for the 'cylinder phantom' could certainly still be improved by simulating more counts to estimate the projector, or by using some optimized filtering of the projector.

### 5.3. Impact of the noise on the projector

Table 5 shows how increasing the number of simulated counts used to estimate the projector reduced the percentage of mislocated events, and improved quantitative accuracy and signal-to-noise ratio. When the number of simulated counts changed from 1 billion to 10 billions, the percentage of mislocated events decreased from 24.9% to 7.7% and the signal-to-noise ratio improved by about 30%. PCA filtering further improved the percentage of mislocated events from 7.7% to 1.7%, and the signal-to-noise ratio by about 6%. These results show the impact of the statistics on the quality of reconstructed images and also stress that high statistics simulations combined with projector filtering should be used to achieve the best results. PCA filtering presents the advantage of acting as a non-parametric adaptive filtering, which does not use any prior knowledge regarding the distribution of the probability values in the projector. Further investigation regarding the projector structure and other filtering approaches are currently under way (Rafecas *et al* 2004).

### 5.4. Robustness of F3DMC as a function of modelling errors

Tables 6 and 7 show that F3DMC results were almost unaffected by a 4 keV error in the energy calibration of the gamma camera ( $P_1$ ). For the 'line and point phantom', results were weakly affected by the 2 mm off-set (representing almost a quarter of a pixel) between the sampling grid used to calculate the projector and the sampling grid used to calculate the projections ( $P_2$ ), but the results strongly deteriorated for a 5 mm off-set (representing half of a pixel) ( $P_3$ ). These results are consistent with the fact that the sources in the 'line and point phantom' were

1 cm thick. For the 'cylinder phantom', results were slightly affected by a 1.56 mm off-set (representing half a pixel), were more affected by a 3.125 mm off-set (representing a pixel) and were strongly affected by a 6.25 mm off-set (representing two pixels). What seems to matter is the absolute off-set between projector and projections expressed in mm, and not in fraction of a pixel. For the simulated tomograph, with a spatial resolution of about 8 mm at 10 cm from the collimator, an off-set greater than 5 mm introduced large quantitative errors in the reconstructed images and also artefacts that can be clearly seen in the reconstructed images. For both phantoms, the impact of modelling errors was similar for F3DMC and MLEM-C, suggesting that F3DMC is as robust as MLEM-C with respect to modelling errors.

Finally, the reconstruction of projections computed with SimSET with a projector computed with GATE demonstrated that when projections and projector were calculated using different tools, reconstructed images were of similar quality (table 7) as when the same model was used for calculating the projections and the projector.

### 5.5. Potentials of F3DMC with respect to alternative reconstruction approaches

Beyond the feasibility and encouraging results of F3DMC reconstruction demonstrated by our results, several original features of F3DMC can be underlined. The major advantage of using a Monte Carlo approach to calculate the projector is that every phenomenon involved in the image formation process can *a priori* be accounted for during the reconstruction, as long as it can be modelled in the Monte Carlo simulations. This includes non-conventional geometric response of a tomograph, which could be useful for non-parallel collimation geometry in SPECT, and in PET where the geometric response of the tomograph is often complex, especially in 3D PET. The very specificity of the patient is also accounted for in F3DMC, as the attenuation map is used to determine the probabilities of the different photon histories for that patient, which makes up the projector. The value of F3DMC reconstruction should also be even more striking for isotopes with several emission energies (e.g., In-111 or I-131), for which the analytical modelling of the camera response is far more complicated than for Tc-99m.

## 6. Conclusion

We have shown the feasibility and potential value of F3DMC reconstruction for SPECT reconstruction on simulated data. F3DMC yielded results as good as or better than other analytical reconstruction approaches, in terms of spatial resolution, quantitative accuracy and signal-to-noise ratios, and appears as robust as other reconstruction methods with respect to modelling errors. One key point in F3DMC reconstruction is the statistical reliability of the projector, which depends on the number of photon histories used to calculate the projector elements. We have introduced a filtering method allowing for noise removal in the projector and demonstrated its efficiency. The next step will be to apply F3DMC to real SPECT data.

## Acknowledgment

This work was supported by the GDR Stic-Santé (France).

## References

- Assié K, Gardin I, Vera P and Buvat I 2005 Validation of the Monte Carlo simulator GATE for indium-111 imaging *Phys. Med. Biol.* **50** 3113–25
- Bai C, Zeng G L and Gullberg G T 2000 A slice-by-slice blurring model and kernel evaluation using the Klein–Nishina formula for 3D scatter compensation in parallel and converging beam SPECT *Phys. Med. Biol.* **45** 1275–307

- Beekman F J, De Jong H W A M and van Geloven S 2002 Efficient fully 3-D iterative SPECT reconstruction with Monte Carlo-based scatter compensation *IEEE Trans. Med. Imaging* **21** 867–77
- Beekman F J, den Harder J M, Viergever M A and van Rijk P P 1997 SPECT scatter modelling in non-uniform attenuating objects *Phys. Med. Biol.* **42** 1133–42
- Beekman F J, Eijkman E G J, Viergever M A, Borm G F and Slijpen E T P 1993 Object shape dependent PSF model for SPECT imaging *IEEE Trans. Nucl. Sci.* **40** 31–9
- Beekman F J, Kamphuis C and Viergever M A 1996 Improved SPECT quantitation using fully three-dimensional iterative spatially variant scatter response compensation *IEEE Trans. Med. Imaging* **15** 491–9
- Beekman F J and Viergever M A 1995 Fast SPECT simulation including object shape dependent scatter *IEEE Trans. Med. Imaging* **14** 271–82
- Bowsher J E and Floyd C E 1991 Treatment of Compton scatter in maximum-likelihood, expectation-maximization reconstruction of SPECT images *J. Nucl. Med.* **32** 1285–91
- Buvat I, Benali H, Todd-Pokropek A and Di Paola R 1994 Scatter correction in scintigraphy: the state of the art *Eur. J. Nucl. Med.* **21** 675–94
- Byrne C L 1996 Block-iterative methods for image reconstruction from projections *IEEE Trans. Med. Imaging* **15** 673–86
- De Jong H W A M, Beekman F J and Slijpen E T P 2001 Acceleration of Monte Carlo SPECT simulation using convolution-based forced detection *IEEE Trans. Nucl. Sci.* **48** 58–64
- Floyd C E, Jaszczak R J and Coleman R E 1989 Inverse Monte Carlo: a unified reconstruction algorithm *IEEE Trans. Nucl. Sci.* **32** 779–85
- Floyd C E, Jaszczak R J, Greer K L and Coleman R E 1986 Inverse Monte Carlo as a unified reconstruction algorithm for ECT *J. Nucl. Med.* **27** 1577–85
- Floyd C E, Jaszczak R J, Manglos S H and Coleman R E 1988 Compensation for collimator divergence in SPECT using inverse Monte Carlo reconstruction *IEEE Trans. Nucl. Sci.* **35** 784–7
- Frey E C, Ju Z W and Tsui B M W 1993 A fast projector-backprojector pair modelling the asymmetric, spatially varying scatter response function for scatter compensation in SPECT imaging *IEEE Trans. Nucl. Sci.* **40** 1192–7
- Frey E C and Tsui B M W 1994 Modelling the scatter response function in inhomogeneous scattering media for SPECT *IEEE Trans. Nucl. Sci.* **41** 1585–93
- Frey E C and Tsui B M W 1996 A new method for modelling the spatially-variant, object dependent scatter response function in SPECT *Conf. Rec. 1996 IEEE Nuclear Science Symposium Medical Imaging Conf. (Piscataway, NJ)* pp 1305–7
- Formiconi A R, Pupi A and Passeri A 1989 Compensation of spatial response in SPECT with conjugate gradient reconstruction techniques *Phys. Med. Biol.* **34** 69–84
- Gilland D R, Jaszczak R J, Wang H, Turkington T G, Greer K L and Coleman R E 1994 A 3D model of non-uniform attenuation and detector response for efficient iterative reconstruction in SPECT *Phys. Med. Biol.* **39** 547–61
- Gilland D R, Tsui B M W, McCartney W H and Perry J R 1988 Determination of the optimum filter function for SPECT imaging *J. Nucl. Med.* **29** 643–50
- Glick S J, Penney B C, King M A and Byrne C L 1994 Noniterative compensation for the distance-dependant detector response and photon attenuation in SPECT imaging *IEEE Trans. Med. Imaging* **13** 363–74
- Harrison R L, Vannoy S D, Haynor D R, Gillipsie S B, Kaplan M S and Lewellen T K 1993 Preliminary experience with the photon generator module of a public-domain simulation system for emission tomography *Conf. Rec. 1993 IEEE Nuclear Science Symp. Med. Imaging Conf. (San Francisco, CA)* pp 1154–58
- Hudson H M and Larkin R S 1994 Accelerated image reconstruction using ordered subsets of projection data *IEEE Trans. Med. Imaging* **13** 601–9
- Jan *et al* 2004 GATE: a simulation toolkit for PET and SPECT *Phys. Med. Biol.* **49** 4543–61
- Jaszczak R J, Greer K L, Floyd C E, Harris C G and Coleman R E 1984 Improved SPECT quantitation using compensation for scattered photons *J. Nucl. Med.* **25** 893–900
- Joliffe I T 1992 Principal component analysis and exploratory factor analysis *Stat. Methods Med. Res.* **1** 69–95
- Kadrmas D J, Frey E C, Karimi S S and Tsui B M W 1998 Fast implementations of reconstruction-based scatter compensation in fully 3D SPECT image reconstruction *Phys. Med. Biol.* **43** 857–74
- Kamphuis C, Beekman F J, Rijk P P and Viergever M A 1998 Dual matrix ordered subsets reconstruction for accelerated 3D scatter compensation in single-photon emission computed tomography *Eur. J. Nucl. Med.* **8**–18
- King M A, Schwinger R B, Doherty P W and Penny B C 1984 Two-dimensional filtering of SPECT images using the Metz and Wiener filters *J. Nucl. Med.* **25** 1234–40
- Lazaro D *et al* 2004 Validation of the GATE Monte Carlo simulation platform for modelling a CsI(Tl) scintillation camera dedicated to small animal imaging *Phys. Med. Biol.* **49** 271–85
- Lewitt R M, Edholm P R and Xia W 1989 Fourier method for correction of depth-dependant collimator blurring *Proc. SPIE* **1092** 232–43

- Miller M I, Snyder D L and Miller T R 1985 Maximum-likelihood reconstruction for single-photon emission computed-tomography *IEEE Trans. Nucl. Sci.* **32** 769–78
- Motta A, Damiani C, Del Guerra A, Di Domenico G and Zavattini G 2002 Use of a fast EM algorithm for 3D image reconstruction with the YAP-PET tomograph *Comput. Med. Imaging Graph.* **5** 293–302
- Munley M T, Floyd C E, Tourassi G D, Bowsher J E and Coleman R E 1991 Out-of-plane photons in SPECT *IEEE Trans. Nucl. Sci.* **38** 776–9
- Ogawa K, Paek S, Nakajima M, Yuta S, Kubo A and Hashimoto S 1988 Correction of collimator aperture using a shift-invariant deconvolution and filter in gamma camera emission CT *Proc. SPIE* **914** 699–706
- Penney B C, King M A and Knesaurek K 1990 A projector, back-projector pair which accounts for the two-dimensional depth and distance dependent blurring in SPECT *IEEE Trans. Nucl. Sci.* **37** 681–6
- Rafecas M, Böning G, Pichler B J, Lorenz E, Schwaiger M and Ziegler S I 2004 Effect of noise in the probability matrix used for statistical reconstruction of PET *IEEE Trans. Nucl. Sci.* **51** 149–56
- Rafecas M, Mosler B, Dietz M, Pögl M, McElroy D P and Ziegler S I 2003 Use of a Monte-Carlo based probability matrix for 3D iterative reconstruction of MADPET-II data *Proc. Conf. Rec. IEEE Nuclear Science Symposium and Medical Imaging Conference 2003 (Portland, USA)*
- Riauka T A, Hooper H R and Gortel Z W 1996 Experimental and numerical investigation of the 3D SPECT photon detection kernel for non-uniform attenuating media *Phys. Med. Biol.* **41** 1167–89
- Shokouhi S, Vaska P, Schlyer D J, Purschke M, Woody C L, Stoll S P, Southehal S and Villanueva A 2004 Statistical 3D image reconstruction for the ratCAP PET tomograph using a physically accurate, Monte Carlo based system matrix *Conf. Rec. 2004 IEEE Nuclear Science Symp. Med. Imaging Conf. (Roma, Italy)* 2M10-136 (CD-ROM)
- Staelens S, Strul D, Santin G, Vandenberghe S, Koole M, D'Asseler Y, Lemahieu I and Van der Walle R 2003 Monte Carlo simulations of a scintillation camera using GATE: validation and application modelling *Phys. Med. Biol.* **48** 3021–42
- Tsui B M W, Gullberg G T, Edgerton E R, Ballard J G, Perry J R, McCartney W H and Berg J 1989 Correction of non-uniform attenuation in cardiac SPECT imaging *J. Nucl. Med.* **30** 497–507
- Tsui B M W, Hu H B, Gilland D R and Gullberg G T 1988 Implementation of simultaneous attenuation and detector response correction in SPECT *IEEE Trans. Nucl. Sci.* **35** 778–83
- Veklerov E, Llacer J and Hoffman E 1988 MLE reconstruction of a brain phantom using a Monte Carlo transition matrix and a statistical stopping rule *IEEE Trans. Nucl. Sci.* **35** 603–7
- Welch A and Gullberg G T 1997 Implementation of a model-based non-uniform scatter correction scheme for SPECT *IEEE Trans. Med. Imaging* **16** 717–26
- Wells R G, Celler A and Harrop R 1998 Analytical calculation of photon distributions in SPECT projections *IEEE Trans. Nucl. Sci.* **45** 3202–14
- Yendiki A and Fessler J A 2004 A comparison of rotation- and blob-based system models for 3D SPECT with depth-dependent detector response *Phys. Med. Biol.* **49** 2157–68
- Zeng G L, Bai C and Gullberg G T 1999 A projector/backprojector with slice-to-slice blurring for efficient three-dimensional scatter modeling *IEEE Trans. Med. Imaging* **18** 722–32
- Zeng G L and Gullberg G T 2000 Unmatched projector/backprojector pairs in an iterative reconstruction algorithm *IEEE Trans. Med. Imaging* **5** 548–55
- Zeng G L, Gullberg G T, Tsui B M W and Terry J A 1991 Three-dimensional iterative reconstruction algorithms with attenuation and geometric point response correction *IEEE Trans. Nucl. Sci.* **38** 693–702